

Article

The Helicity of Magnetic Fields Associated with Relativistic Electron Vortex Beams

Norah Alsaawi ^{1,2,*}  and Vasileios E. Lembessis ² ¹ Department of Physics, College of Science, Qassim University, P.O. Box 6644, Buraidah 51452, Saudi Arabia² Department of Physics and Astronomy, College of Science, King Saud University, P.O. Box 2455, Riyadh 11451, Saudi Arabia; vlempeis@ksu.edu.sa

* Correspondence: no.alsaawi@qu.edu.sa

Abstract: For radially extended Bessel modes, the helicity density distributions of magnetic fields associated with relativistic electron vortex beams are investigated for first time in the literature. The form of the distribution is defined by the electron beam's cylindrically symmetric density flux, which varies with the winding number ℓ and the electron spin. Different helicity distributions are obtained for different signs of the winding number $\pm\ell$, confirming the chiral nature of the magnetic fields associated with the electron vortex beam. The total current helicity for the spin-down state is smaller than that of the spin-up state. The different fields and helicities associated with opposite winding numbers and/or spin values will play an important role in the investigation of the interaction of relativistic electron vortices with matter and especially chiral matter. A comparison of the calculated quantities with the corresponding ones in the case of non-relativistic spin-polarized electron beams is performed.

Keywords: vortex beams; electrons; helicity; chirality; current density



Citation: Alsaawi, N.; Lembessis, V.E. The Helicity of Magnetic Fields Associated with Relativistic Electron Vortex Beams. *Symmetry* **2024**, *16*, 496. <https://doi.org/10.3390/sym16040496>

Academic Editor: Wiesław Leonski

Received: 2 March 2024

Revised: 9 April 2024

Accepted: 11 April 2024

Published: 19 April 2024



Copyright: © 2023 by the authors. Licensee MDPI, Basel, Switzerland. This article is an open access article distributed under the terms and conditions of the Creative Commons Attribution (CC BY) license (<https://creativecommons.org/licenses/by/4.0/>).

1. Introduction

Electron vortex modes as twisted electron beams have been experimentally realized in recent years [1–3]. These beams of freely propagating electrons have a wavefront with a quantized topological structure, and they can carry large amounts of quantum angular momentum equal to $\ell\hbar$ in the direction of propagation [4]. This wavefront arises from a singularity in phase that takes the form $e^{i\ell\phi}$, where ϕ represents the azimuthal angle about the beam axis and ℓ is an integer quantum number that is also referred to as the topological charge (or winding number). The fundamental ideas behind electron vortex beam production are roughly the same as those found in the optical vortex counterparts; however, the electron vortex is unique due to a few more characteristics, most notably its electric charge, mass, half-integer spin, and extremely small de Broglie wavelengths. Lloyd et al. [5] studied the behaviour of the electromagnetic field of a non-relativistic electron vortex Bessel beam.

The applications of electron vortices span in large areas range from quantum information and nuclear physics up to nanoscience. For example, they provide useful new information about the magnetic properties of matter using electron energy-loss spectroscopy [2], and we can exploit them in the determination of the chirality of crystals in transmission electron microscopy [6]. The application of electron vortex beams with varying handedness, $+\ell$ or $-\ell$, causes distinct reactions in chiral matter, that is, the relative handedness of the electron vortex beam affects interaction processes [6–9]. Several studies have examined high-energy processes, such as radiation generated by an electron vortex, Compton scattering, and Mott scattering. This requires a fully relativistic treatment of electrons; therefore, the Dirac equation instead of the Schrödinger equation should be considered [4,10]. Difficult quantity measurements, previously unexplored in particle or nuclear collisions, have been accessed via relativistic vortex electrons [11]. Attempts for an exact solution to the Dirac equation

for an electron vortex have been performed in a number of studies, either for electrons that propagate in free space or interact with a laser field, a homogeneous magnetic field, or more general field configurations (see review [12] and the references therein).

The helicity associated with electron vortex beams, both magnetic and current, is our main focus here. Helicity, defined as the linking or twisting of field lines [13,14], is a mathematical tool for evaluating the handedness of magnetic fields. The study of helicity was motivated by its potential applications in a variety of contexts such as gravitational waves [15], magnetohydrodynamics, magnetic reconnection, astronomy studies [16,17] (e.g., active galactic regions and planetary magnetospheres), and light propagation through dispersive and negative-index media [18] (for overviews see [19,20]). The helicity and chirality of the electromagnetic fields associated with optical vortex beams have recently been the subject of investigation and clarification [21,22]. These characteristics are critical for understanding how chiral light interacts with matter. Furthermore, a thorough understanding of the material's characteristics can be obtained by utilizing electron vortex beams with various spin polarization and helicity density values. In this paper, we plan to investigate in detail the helicities of the magnetic fields associated with a relativistic electron vortex beam in a way analogous to that followed in the study of non-relativistic electron vortex beams [23].

We adopted a Bessel-type solution of the Dirac equation, first provided by Bliokh et al. [24], which describes a fully relativistic vortex of electrons with spin. Barnett [25] suggested the approximate paraxial Laguerre–Gaussian beam as an alternative solution to the Dirac equation, which acquires non-paraxial corrections to accurately analyze spin–orbit interaction effects. These corrections introduce additional components with different vortex charges and spin projections, but only one of these components is present in their work. The authors of [26] proposed exponential wave packets localized in time but extending indefinitely along the longitudinal z coordinate. While they may not precisely represent longitudinally-localized electron wave packets in typical experimental conditions, they can be useful in situations where the finite width of the electron energy spectrum is important. Indeed, choosing the Bessel-type solution of the Dirac equation is generally more realistic, and it gives us the opportunity to compare the relativistic results with those obtained for non-relativistic spin-polarized electron vortex beams [23]. The electromagnetic fields generated by a relativistic electron vortex beam have been proposed recently by Lei et al. [27], where they depend on both the spin state and the winding number.

In this paper, we aim to identify the current and magnetic helicity densities of magnetic fields associated with a relativistic electron vortex beam. The structure of the paper is as follows. In Section 2, we give the wave function of the relativistic electron vortex beam and the expressions for the components of its magnetic field. Section 3 discusses the properties of the current and magnetic helicities adopting a Bessel-type solution for the Dirac equation. The non-relativistic limit of the results is presented in Section 4. Finally, in Section 5, we give our conclusions.

2. Relativistic Electron Vortex Beams

As mentioned in the introduction, the relativistic behavior exhibited by an electron vortex is described by the Dirac equation and has been shown by Bliokh et al. [24]. The wave function for an electron propagating along the z direction takes the following

$$\psi_{l,s} = \frac{N_l e^{i(k_z z - \omega t)}}{\sqrt{2}} \left[\left(\frac{\sqrt{1 + \frac{m_e c^2}{E}} w_s}{\sqrt{1 - \frac{m_e c^2}{E}} \sigma_z \cos \theta w_s} \right) J_\ell(k_\perp \rho) e^{i\ell\phi} + i \begin{pmatrix} 0 \\ 0 \\ -b\sqrt{\Delta} \\ 0 \end{pmatrix} e^{i(\ell-1)\phi} J_{\ell-1}(k_\perp \rho) + i \begin{pmatrix} 0 \\ 0 \\ 0 \\ a\sqrt{\Delta} \end{pmatrix} e^{i(\ell+1)\phi} J_{\ell+1}(k_\perp \rho) \right], \quad (1)$$

where N_ℓ is the normalization constant, c is the speed of light, m_e is the mass of the electron, E is the electron beam energy, σ_z is the z component of the Pauli matrix, $\theta = \tan^{-1}(k_\perp/k_z)$ is the opening angle of the cone of the Bessel plane defined in terms of wave vector components, $\Delta = \sin^2 \theta (1 - \frac{m_e c^2}{E})$ is the spin-orbit coupling strength, $J_\ell(k_\perp \rho)$ is the first-order Bessel function, $w_s = (a, b)^T$ is the spin state with $|a|^2 + |b|^2 = 1$, and s represents the electron spin with values $\pm \frac{1}{2}$ characterizing the eigenstate of the Pauli operator s_z . Here, we assume such states $w_{\frac{1}{2}} = (1, 0)^T$ for spin 'up' and $w_{-\frac{1}{2}} = (0, 1)^T$ for spin 'down'. Furthermore, in the following numerical evaluation, the wave vector component values are assumed to be $k_\perp = 2.3 \times 10^8 \text{ m}^{-1}$ and $k_z = 2.3 \times 10^{12} \text{ m}^{-1}$. This ensures that $\theta = 0.1$ mrad is in agreement with experiments in MeV electron microscopy/diffraction [28], where the electron beam energy is equal to 2 MeV. Applying the normalization procedure for the wave function Equation (1) leads to $|N|^2 = \frac{k_\perp}{4\pi^2}$ for an infinite radial extent Bessel beam. In the non-relativistic limit, the quantity Δ that describes the intrinsic spin-orbit interaction vanishes and θ takes small values. The four-current density in relativistic electromagnetic theory is written as

$$\mathbf{J}^\alpha = (c\rho, j^1, j^2, j^3) = (c\rho, \mathbf{j}), \quad (2)$$

where ρ stands for the charge density, and \mathbf{j} is the current density. The charge and current densities in the Bessel mode wave function, given in Equation (1), have previously been shown by Bliokh et al. [24] as follows:

$$\rho_{l,s}(\mathbf{r}) = -eN_\ell^2 \left[\left(1 - \frac{\Delta}{2}\right) J_\ell^2(k_\perp \rho) + \frac{\Delta}{2} J_{\ell+2s}^2(k_\perp \rho) \right], \quad (3)$$

$$\mathbf{j}_{l,s} = \frac{-eN_\ell^2 \hbar k c^2}{E} (J_\ell^2(k_\perp \rho) \cos \theta \hat{z} + J_\ell(k_\perp \rho) J_{\ell+2s}(k_\perp \rho) \sin \theta \hat{\phi}). \quad (4)$$

As we can clearly see from the two above equations, the introduction of spin degrees of freedom in the relativistic regime brings in modifications in the charge and current densities, and this will lead to different magnetic field expressions for the two spin states and helicities associated with these fields. The physical reason for this is that in the non-relativistic regime, the orbital angular momentum and the spin angular momentum are separately conserved. In this case the wave function, for a particle in free space, is just a product of the coordinate and spin parts. This has to be contrasted with the relativistic case, where the conserved quantity is the total angular momentum since, even in free space, the spin is coupled to the orbital angular momentum [26]. The helical trajectories of the current density lead the electron vortex to possess intrinsic magnetic fields expressed in cylindrical coordinates. The relativistic electric and magnetic field components may now be found using the four-current density in the inhomogeneous Maxwell equation $\partial_\beta \mathbf{F}^{\alpha\beta} = -\mu_0 \mathbf{J}^\alpha$ for infinite radial extent Bessel beams, leading to [27]

$$E(\rho) = -\hat{\rho} \frac{eN_\ell^2}{\epsilon_0 \rho} \int_0^\rho \left[J_\ell^2(k_\perp \rho') + \frac{\Delta}{2} (J_{\ell+2s}^2(k_\perp \rho') - J_\ell^2(k_\perp \rho')) \right] \rho' d\rho', \quad (5)$$

$$B_\phi(\rho) = \frac{eN_\ell^2 \mu_0 \hbar k_z c^2}{E \rho} \int_0^\rho J_\ell^2(k_\perp \rho') \times \rho' d\rho', \quad (6)$$

$$B_z(\rho) = \frac{eN_\ell^2 \mu_0 \hbar k_\perp c^2}{E} \int_\rho^\infty J_\ell(k_\perp \rho') J_{\ell+2s}(k_\perp \rho') d\rho', \quad (7)$$

where $k_z = k \cos \theta$ and $k_\perp = k \sin \theta$. The azimuthal magnetic field component does not depend on the spin, it is almost identical to the non-relativistic one [5] with a slight difference in the constant involved. It has been demonstrated that it exhibits an oscillatory form that reduces with increasing radial distance and whose amplitude decreases with increasing winding number. Its formula incorporates the Bessel function of the first kind

squared; hence, it is independent of the winding number's sign. The oscillating feature is a direct effect of the oscillating nature of the Bessel beam. On the contrary, the axial component depends explicitly on the spin quantum number, where it takes lower values in the case of spin-down states compared to spin-up states. Additionally, the axial magnetic fields associated with electron vortex beams with various spin states converge to common values as the winding number increases. The axial magnetic field component for a spin-up electron vortex beam with $\ell = -1$ is opposite to that of a spin-down vortex with $\ell = 1$. This is in agreement with what we found in the case of a non-relativistic spin-polarized electron vortex beam [23].

3. Helicity Density

Moreau [13] and Moffatt [14] showed that the vortex lines of flows with a non-zero total helicity are both knotted and linked. A pseudoscalar 'helicity' integral of the form $\mathbf{u} \cdot (\nabla \times \mathbf{u}) d^3x$ can be associated with the topological properties of the field lines, in other words, helicity can be considered as a topological measure of how much the field lines wrap and coil around the propagation axis. This property applies to both the vector potential \mathbf{A} and magnetic field \mathbf{B} [29,30], and it gives rise to their definitions of the corresponding helicity densities: the current helicity density χ can be defined as

$$\chi = \mathbf{B} \cdot (\nabla \times \mathbf{B}), \quad (8)$$

and the magnetic helicity density η can be defined as

$$\eta = \mathbf{A} \cdot (\nabla \times \mathbf{A}) = \mathbf{A} \cdot \mathbf{B}. \quad (9)$$

We may infer that the magnetic field and vector potential components are solely functions of the radial distance thanks to the Bessel mode and the cylindrical symmetry consideration. As a result, the components along the radial direction and their derivatives with respect to ϕ and z vanish.

3.1. Current Helicity Density

Substituting the relativistic magnetic field expressions in Equations (6) and (7) into Equation (8) leads to

$$\chi = \frac{e^2 c^4 \mu_0^2 \hbar^2 k_z k_\perp |N_\ell|^4}{E^2 \rho} \left(\int_\rho^\infty J_\ell(k_\perp \rho') J_{\ell+2s}(k_\perp \rho') d\rho' \times \frac{\partial}{\partial \rho} \left(\int_0^\rho J_\ell^2(k_\perp \rho') \rho' d\rho' \right) - \int_0^\rho J_\ell^2(k_\perp \rho') \rho' d\rho' \times \frac{\partial}{\partial \rho} \left(\int_\rho^\infty J_\ell(k_\perp \rho') J_{\ell+2s}(k_\perp \rho') d\rho' \right) \right). \quad (10)$$

The radial distribution of the current helicity density results for beams of order $\ell = 0, \pm 1$, and ± 10 are illustrated in Figure 1. It can be seen that the current helicity density has an oscillating structure similar to that of the magnetic field components. As we increase the winding number, we obtain a lower first peak and diminishing oscillations at longer radial distances ρ . The non-vanishing χ for the case of $\ell = 0$ is noteworthy here, where the plots for the two different values of s are mirror images with respect to the horizontal axis. The plots for $\ell > 0$ exhibit noticeably different characteristics; for example, the plots (b) (spin-up) and (d) (spin-down) for beams with $|\ell| = 1$ look symmetrical with respect to the z -axis, and the same holds for $|\ell| = 10$. Based on the magnetic field formulas and the Bessel function property $J_{-\ell}(x) = (-1)^\ell J_\ell(x)$, which holds for integer ℓ [31], this indicates that $J_\ell = J_{-\ell}$ for even ℓ , and $J_\ell = -J_{-\ell}$ for odd ℓ . We infer that for negative winding numbers, both the current helicity density and total current helicity of the spin-up state become opposite to the spin-down-state.

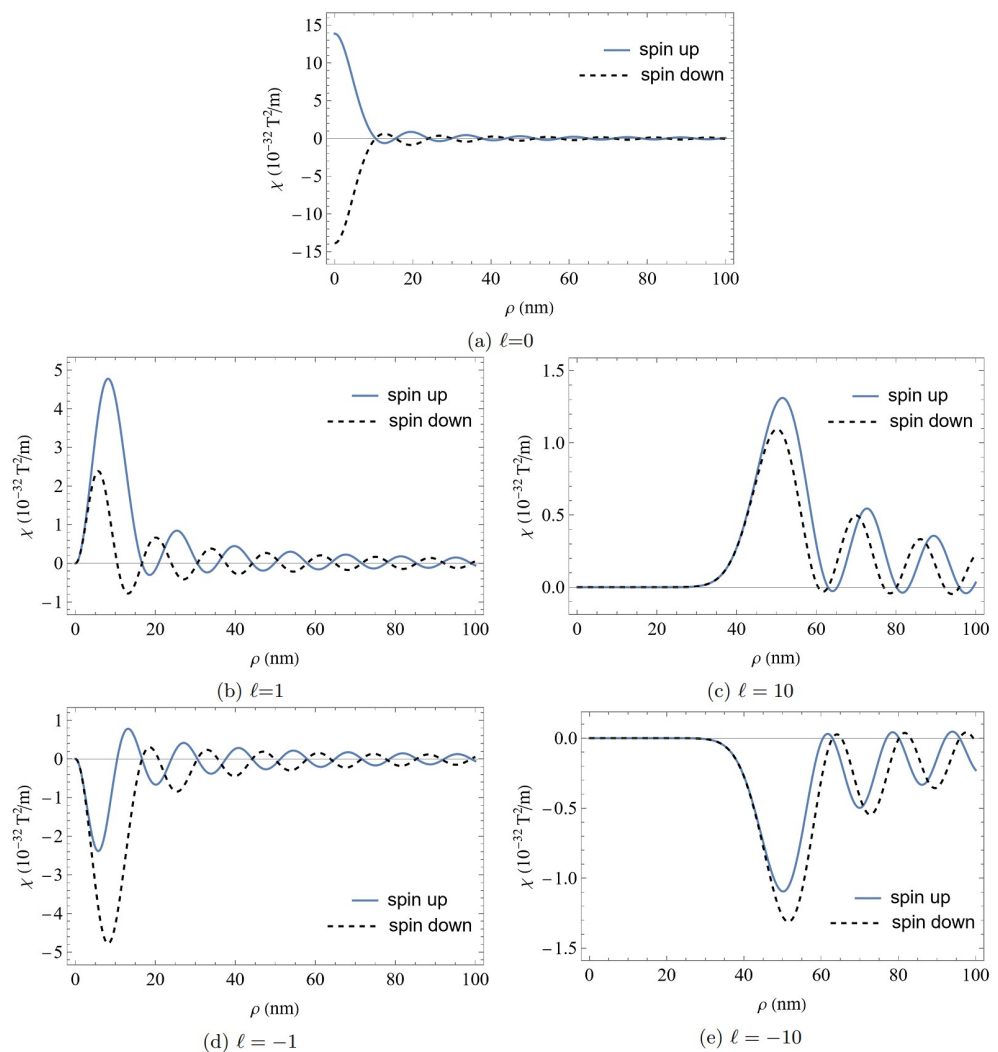


Figure 1. The current helicity density of an infinite relativistic electron Bessel beam with (a) $\ell = 0$, (b) $\ell = 1$, (c) $\ell = 10$, (d) $\ell = -1$, and (e) $\ell = -10$. The radial oscillatory behaviour dominates at larger radial distances for a higher winding number associated with a lower current helicity value.

In Figure 2, we see the two-dimensional distribution of the current helicity density, which gives a clearer visualization of the difference between the two spin states. It is also easy to deduce from Figure 2c,e that the distributions of $\ell = \pm 1$ with the same spin value cannot be described as mirror images of each other. The regions of low current helicity density (shown in blue) in Figure 2c replace the high helicity density (bright yellow) of the focal plane; however, their magnitudes are not identical. This is clearly shown in Equation (10), in which the current helicity density relies on the spin states and sign of ℓ . These findings confirm the chiral character of the relativistic electron vortex beam, similar to what has been observed in the case of non-relativistic spin-polarized electron vortex beams [23]. The choice of a lower value of the radial wave vector in this relativistic treatment causes a larger radial spread for all the components of the field, and hence this holds for the current and magnetic helicity densities compared to the non-relativistic case. This is expressed by the multiplication of the radial wave vector and the radial distance ρ in the argument of the Bessel function.

An integration across the full transverse plane yields the total current helicity per unit length as

$$\mathcal{H}_C = \int_S \mathbf{B} \cdot (\nabla \times \mathbf{B}) \rho d\rho d\phi, \quad (11)$$

where the integration over ϕ gives 2π . Using Mathematica's Double Exponential Oscillatory numerical integration approach, the total current helicity for each ℓ value was determined for the range $\ell = -10$ to $\ell = 10$. These results are shown in Figure 3. Interestingly, we find that for $\ell = 0$, the spin contribution coming from relativistic effects prevents the total helicity from being zero. The outcome is not wholly unexpected because the charge and current distributions, which are what cause all of the physical effects in this work, have a cylindrical symmetry. Therefore, the J_z eigenvalue along the z -axis, rather than the total angular momentum J or OAM ℓ , is what matters in this situation. As the winding number increases, the total current helicity increases for both spin states and is larger in the spin-up state. The difference between the total current helicities of the two opposite spin relativistic vortex beams is not constant and varies slightly as a function of the winding number ℓ .

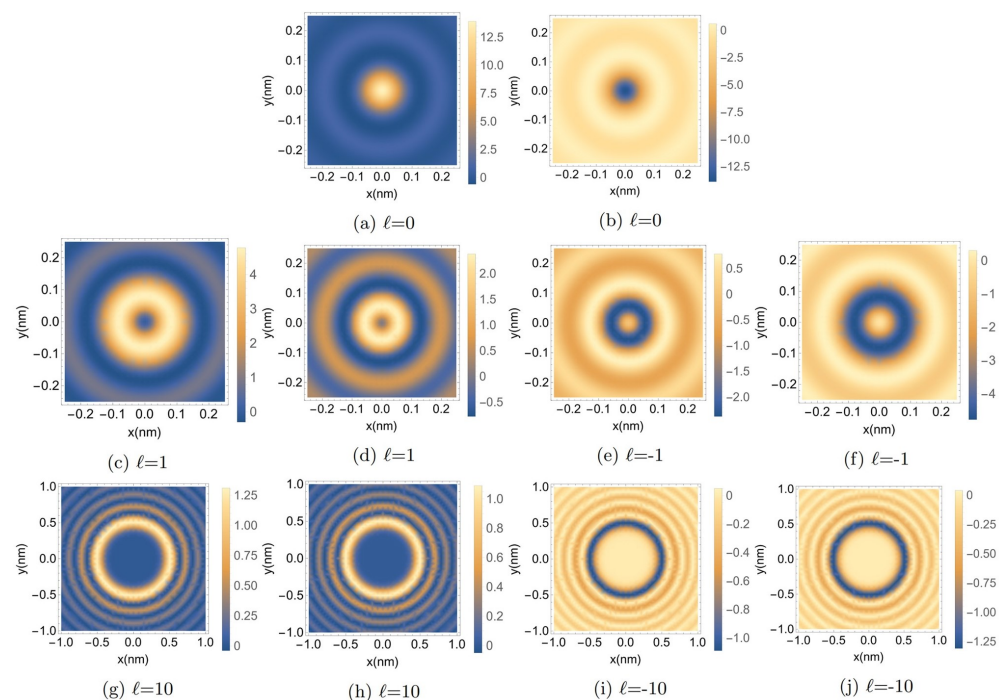


Figure 2. The in-plane current helicity density distribution for an infinite relativistic electron Bessel beam with (a) $\ell = 0$, (c) $\ell = 1$, (e) $\ell = -1$, (g) $\ell = 10$, and (i) $\ell = -10$ in the case of spin-up. The corresponding plots in the case of spin-down are illustrated for the winding number with (b) $\ell = 0$, (d) $\ell = 1$, (f) $\ell = -1$, (h) $\ell = 10$, and (j) $\ell = -10$.

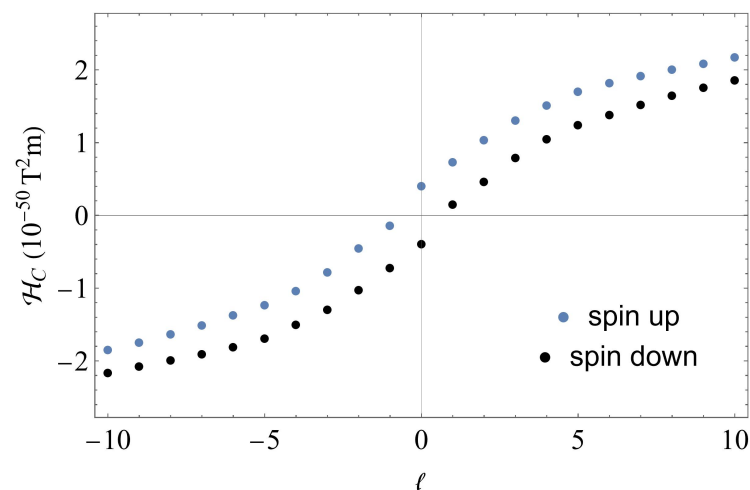


Figure 3. The total current helicity for an infinite relativistic electron Bessel beam from $\ell = -10$ to $\ell = 10$ in spin-up and spin-down states.

3.2. Magnetic Helicity Density

The previously calculated magnetic field expressions in Equations (6) and (7) are used in a direct evaluation of the vector potential of the relativistic electron vortex beam. These magnetic field components are related to the vector potential components in the following way in cylindrical coordinates:

$$\mathbf{B} = -\frac{dA_z}{d\rho}\hat{\boldsymbol{\phi}} + \frac{1}{\rho}\frac{d(\rho A_\phi)}{d\rho}\hat{\mathbf{z}}. \quad (12)$$

Inserting the relativistic magnetic field expressions, one obtains two differential equations:

$$\frac{dA_z}{d\rho} = -\frac{eN_\ell^2\mu_0\hbar kc^2 \cos\theta}{E\rho} \int_0^\rho J_\ell^2(k_\perp\rho) \times \rho d\rho, \quad (13)$$

$$\frac{1}{\rho}\frac{d(\rho A_\phi)}{d\rho} = \frac{eN_\ell^2\mu_0\hbar k_\perp c^2}{E} \int_\rho^\infty J_\ell(k_\perp\rho)J_{\ell+2s}(k_\perp\rho)d\rho, \quad (14)$$

the last equation can be written as

$$\frac{dA_\phi}{d\rho} + \frac{A_\phi}{\rho} = \frac{eN_\ell^2\mu_0\hbar k_\perp c^2}{E} \int_\rho^\infty J_\ell(k_\perp\rho)J_{\ell+2s}(k_\perp\rho)d\rho, \quad (15)$$

where working out the integration, we find

$$\frac{dA_\phi}{d\rho} + \frac{A_\phi}{\rho} = \frac{eN_\ell^2\mu_0\hbar c^2}{E} \begin{cases} \left[\frac{1}{2} - \frac{{}_2F_3[\{\ell+1, \ell+\frac{3}{2}\}; \{\ell+2, \ell+2, 2\ell+2\}; -\rho^2 k_\perp^2] 4^{-\ell} (\rho k_\perp)^{2\ell+2}}{4\Gamma^2(\ell+2)} \right]; \text{ if } s = \frac{1}{2} \\ \left[\frac{1}{2} - \frac{{}_2F_3[\{\ell, \ell+\frac{1}{2}\}; \{2\ell, \ell+1, \ell+1\}; -\rho^2 k_\perp^2] 4^{-\ell} (\rho k_\perp)^{2\ell}}{\Gamma^2(\ell+1)} \right]; \text{ if } s = -\frac{1}{2}. \end{cases} \quad (16)$$

Solving Equations (13) and (16) using Mathematica's built-in function DSolve for the solution of the first-order differential equations, we obtain

$$A_\phi(\rho) = \frac{eN_\ell^2\mu_0\hbar c^2\rho}{2k_\perp E} \begin{cases} \left[\frac{1}{2} - {}_2\tilde{F}_3[\{\ell+1, 2\ell+\frac{3}{2}\}; \{\ell+2, 2\ell+2, \ell+3\}; -\rho^2 k_\perp^2] \Gamma(2+2\ell) 4^{-\ell} (\rho k_\perp)^{2\ell+2} \right]; \text{ if } s = \frac{1}{2} \\ \left[\frac{1}{2} - {}_2\tilde{F}_3[\{\ell, \ell+\frac{1}{2}\}; \{2\ell, \ell+1, \ell+2\}; -\rho^2 k_\perp^2] \Gamma(2\ell) 4^{-\ell} (\rho k_\perp)^{2\ell} \right]; \text{ if } s = -\frac{1}{2} \end{cases}, \quad (17)$$

$$A_z(\rho) = \frac{e\mu_0\hbar|N_\ell|^2 k_z c^2 \rho^2}{4E} [J_{\ell-1}(k_\perp\rho)J_{\ell+1}(k_\perp\rho) - J_{\ell+1}^2(k_\perp\rho) - J_\ell^2(k_\perp\rho) + J_\ell(k_\perp\rho)J_{\ell+2}(k_\perp\rho) + 4^{-\ell} (\rho k_\perp)^{2\ell} \Gamma(2+2\ell) {}_2\tilde{F}_3[\{1+\ell, \frac{3}{2}+\ell\}; \{2+\ell, 2+\ell, 2+2\ell\}; -\rho^2 k_\perp^2]]. \quad (18)$$

where ${}_p\tilde{F}_q[a_1\dots a_p; b_1\dots b_q; z]$ is the regularized hypergeometric function. In Appendix A we show that this set of vector potential components satisfies the Coulomb gauge condition $\nabla \cdot \mathbf{A} = 0$. We can test that they reproduce the correct magnetic field components by taking the curl of the vector potential in cylindrical coordinates.

After substituting them into the magnetic helicity density given in Equation (9), we can generate Figures 4 and 5, which show the densities and their distribution for winding numbers $\ell = 0, \pm 1$ and ± 10 . In case of a zero winding number, the spin-up magnetic helicity is the inverse of the spin-down magnetic helicity; however, for a given non-zero OAM, the spin-down Bessel vortex beam's magnetic helicity is always smaller than the spin-up Bessel vortex beam's, and the difference between the two becomes smaller with larger ℓ values. Increasing the winding number will increase the magnetic helicity density value and radial extend of the region around the vortex core, where the helicity density is zero. All these features were observed in the magnetic helicity density associated with the non-

relativistic spin-polarized electron vortex beam [23]. As we pointed out in the discussion about current helicity, the difference is related to their current density expressions and chosen values for the wave vector components.

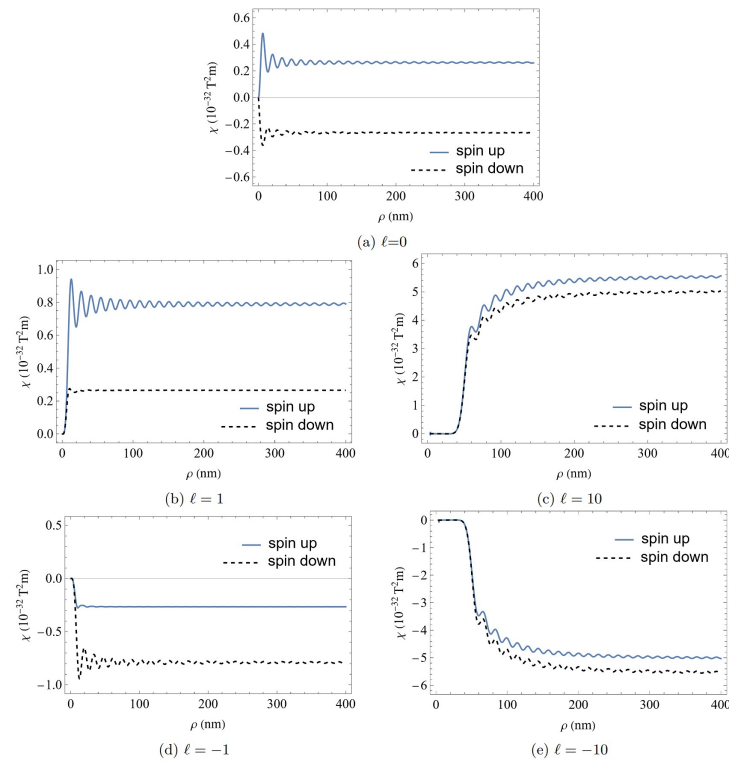


Figure 4. The magnetic helicity density of an infinite relativistic electron Bessel beam with (a) $\ell = 0$, (b) $\ell = 1$, (c) $\ell = 10$, (d) $\ell = -1$, and (e) $\ell = -10$. The difference between the magnetic helicity densities of the two spin states is clearly demonstrated. The height of the first peak increases for higher values of ℓ .

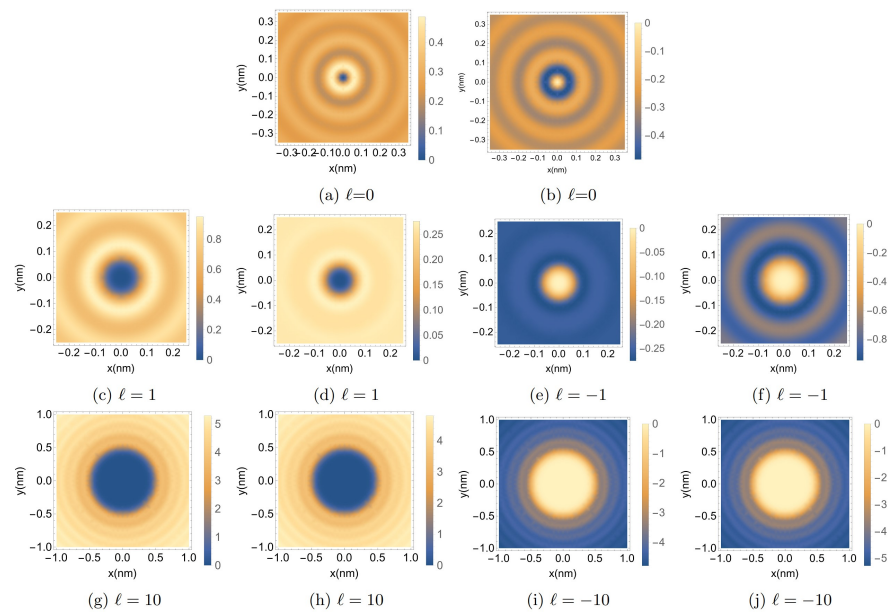


Figure 5. The in-plane magnetic helicity density distribution for an infinite relativistic electron Bessel beam with (a) $\ell = 0$, (c) $\ell = 1$, (e) $\ell = -1$, (g) $\ell = 10$, and (i) $\ell = -10$ in the case of spin-up. The corresponding plots in the case of spin-down are illustrated for the winding number with (b) $\ell = 0$, (d) $\ell = 1$, (f) $\ell = -1$, (h) $\ell = 10$, and (j) $\ell = -10$.

4. Non-Relativistic Limit

The energy–momentum relation is given by $E^2 = p^2c^2 + m^2c^4$, where m is the rest mass or invariant mass for an electron; this expression reduces to $E = mc^2$ in the low velocities limit ($p \rightarrow 0$) [24]. Accordingly, the previous magnetic field expressions in Equations (6) and (7) take the form

$$B_\phi(\rho) = \frac{eN_\ell^2\mu_0\hbar k_z}{m_e\rho} \int_0^\rho J_\ell^2(k_\perp\rho') \times \rho' d\rho', \quad (19)$$

$$B_z(\rho) = \frac{eN_\ell^2\mu_0\hbar k_\perp}{m_e} \int_\rho^\infty J_\ell(k_\perp\rho') J_{\ell+2s}(k_\perp\rho') d\rho'. \quad (20)$$

The value $k_z = 2.3 \times 10^{12} \text{ m}^{-1}$ for the longitudinal momentum is utilized in the numerical evaluation that follows. This value corresponds to an accelerating voltage of 300 keV, which is typical for electron microscopes used in electron vortex beam experiments [2]. The transverse wave vector component k_\perp was assumed to be two orders of magnitude larger than the transverse wave vector component k_\parallel , or $2.3 \times 10^{10} \text{ m}^{-1}$ [5]. By substituting the magnetic field expressions in the non-relativistic limit (Equations (19) and (20)) in the current helicity density given in Equation (8), we obtained the results illustrated in Figure 6 for $\ell = 0, 1$ and 10. These plots are exactly the same as the corresponding plots found previously in the case of non-relativistic spin-polarized electron vortex beams [23]. A similar results is expected for the magnetic helicity density plots in the non-relativistic limit. Since the magnetic helicity density is derived from vector potential components that are obtained from the magnetic field, their plots in the non-relativistic limit will agree with the ones taken for the non-relativistic spin-polarized electron vortex beams. Our numerical work has shown that if we obtain the formalism of the non-relativistic case, use the relativistic values for k_z , k_\perp , and then instead of the electron mass we use its invariant mass expression, then the results we obtain will be identical to the ones we have in this paper. This is a clear indication that the mass increase that occurs in the relativistic velocities is responsible for the reduction in the calculated quantities compared to the ones in the non-relativistic regime.

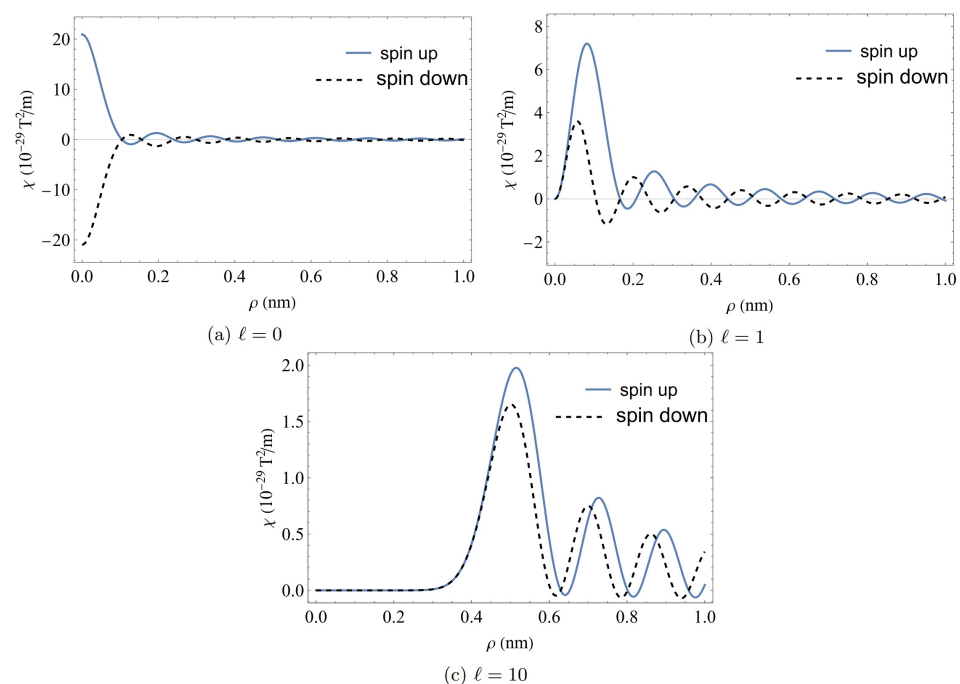


Figure 6. The current helicity density of an infinite relativistic electron Bessel beam with (a) $\ell = 0$, (b) $\ell = 1$, and (c) $\ell = 10$ within the limit of small velocities.

5. Conclusions

In summary, to the best of our knowledge, we have, for the first time, investigated the magnetic and current helicity densities of magnetic fields associated with a Bessel-type relativistic electron vortex beam. Their dependence on the winding number of the electron vortex beam was highlighted. It was found that the azimuthal magnetic field component of the relativistic Bessel beam is the same as that of the non-relativistic one, while different axial magnetic field values were observed for the two spin states. This caused a difference in the magnetic and current helicity density results associated with the spin-up and spin-down relativistic electron vortex beams, which are shown in the corresponding plots in agreement with what was previously found in the case of non-relativistic spin-polarized electron vortex beams [23]. We must point out that the resulting values of the relativistic current helicity density are about three orders of magnitude lower compared to the non-relativistic ones. However taking the non-relativistic limit of the magnetic field expressions together with the assumption that the transverse wave vector component is two orders of magnitude smaller than the axial wave vector (which is used in the non-relativistic treatment), lead us to assume that the current and magnetic helicity density plots are identical to those obtained for a non-relativistic treatment of a spin-polarized electron vortex beam.

By comparing the distribution plots for opposite winding numbers, we have demonstrated that the fields associated with relativistic electron vortex beams have helicity and exhibit chirality. In terms of helicity, there has been a lot of work published in recent years investigating novel optical forces that can arise when a chiral particle is exposed to a chiral light field. These new forces depend on the chirality of the optical field that produces them, as well as the chirality of the system they act upon [32]. Furthermore, since the electron vortex fields are chiral, chiral materials can be identified and analyzed, yielding details on their spatial organization, structural characteristics, and possible biological or chemical activities. Furthermore, advances in quantum computing and communications may result from the encoding and processing of quantum information via chirality. To completely comprehend and make use of the potential of these chiral characteristics, more research and experimental studies are required.

In our work, we have also derived an expression for the vector potential components to investigate the magnetic helicity density. We showed that when the winding number is increased, the position of the first peak of the current helicity density is shifted towards a larger radial distance and increase in value. We also calculated the total current helicity and emphasised that the spin-up total helicity equal minus that of the spin-down for opposite winding numbers. The helicities for various spin values will converges when ℓ increases, this suggests that when the OAM increases, its contribution to the current density becomes more and more dominant over the one which stems from the electron spin.

Finally, it is interesting to discuss our findings about the helicity of electron vortices that have half-integer spin compared with their respective counterparts for optical vortices with integer spin. As has been showed in recent work [33], the total helicity of a circularly polarized optical vortex beam is proportional to the optical spin σ and depends on the absolute value of the winding number $|\ell|$. As a result, the sign of the total helicity is determined solely by the sign of the spin of the beam. In an electron vortex beam, the total helicity of the magnetic field depends both on the winding number ℓ and the spin, as is clearly shown in Figure 3. Moreover, the total helicity of an optical vortex is only different than zero when the beam is strongly focused and its electromagnetic field contains a longitudinal component of magnitude considerable to the transverse ones. We believe that these findings could contribute to a better understanding of half-spin vortex beams.

Author Contributions: Conceptualization, N.A. and V.E.L.; formal analysis, N.A.; funding acquisition, N.A.; investigation, N.A.; resources, N.A.; supervision, V.E.L.; validation, V.E.L.; writing—original draft, N.A. All authors have discussed the results and contributed equally to the final manuscript. All authors have read and agreed to the published version of the manuscript.

Funding: This research was funded by the Deanship of Scientific Research, Qassim University.

Data Availability Statement: The original contributions presented in the study are included in the article, further inquiries can be directed to the corresponding authors.

Acknowledgments: The researchers would like to thank the Deanship of Scientific Research, Qassim University, for funding the publication of this project.

Conflicts of Interest: The authors declare no conflicts of interest.

Appendix A

We expanded the vector potential divergence in cylindrical coordinates by

$$\left(\frac{1}{\rho} \frac{\partial}{\partial \rho} \left(\rho \frac{\partial}{\partial \rho}\right)\right) A_{\rho} + \frac{1}{\rho} \frac{\partial}{\partial \phi} A_{\phi} + \frac{\partial}{\partial z} A_z. \quad (\text{A1})$$

We have the zero radial component of the vector potential as it appears from A_{ϕ} and A_z given in Equations (17) and (18); they are only functions of ρ , so the second and third terms vanish. The cylindrical symmetry of the problem imposes that the vector potential, concerning the magnetic and electric fields, does not depend upon ϕ or z to be consistent with the components of the magnetic field, and therefore the vector potential has the same dependence as the current density [34]. Hence, the Coulomb gauge $\nabla \cdot \mathbf{A} = 0$ holds.

References

1. Uchida, M.; Tonomura, A. Generation of electron beams carrying orbital angular momentum. *Nature* **2010**, *464*, 737–739. [CrossRef] [PubMed]
2. Verbeeck, J.; Tian, H.; Schattschneider, P. Production and application of electron vortex beams. *Nature* **2010**, *467*, 301–304. [CrossRef] [PubMed]
3. McMorran, B.; Agrawal, A.; Anderson, I.; Herzing, A.; Lezec, H.; McClelland, J.; Unguris, J. Electron vortex beams with high quanta of orbital angular momentum. *Science* **2011**, *331*, 192–195. [CrossRef] [PubMed]
4. Bliokh, K.Y.; Ivanov, I.P.; Guzzinati, G.; Clark, L.; Boxem, R.V.; Béché, A.; Juchtmans, R.; Alonso, M.A.; Schattschneider, P.; Nori, F.; et al. Theory and applications of free-electron vortex states. *Phys. Rep.* **2017**, *690*, 1–70. [CrossRef]
5. Lloyd, S.; Babiker, M.; Yuan, J.; Kerr-Edwards, C. Electromagnetic vortex fields, spin, and spin-orbit interactions in electron vortices. *Phys. Rev. Lett.* **2012**, *109*, 254801. [CrossRef] [PubMed]
6. Juchtmans, R.; Béché, B.; Abakumov, A.; Batuk, M.; Verbeeck, J. Using electron vortex beams to determine chirality of crystals in transmission electron microscopy. *Phys. Rev.* **2015**, *91*, 094112. [CrossRef]
7. Lloyd, S.; Babiker, M.; Yuan, J. Quantized orbital angular momentum transfer and magnetic dichroism in the interaction of electron vortices with matter. *Phys. Rev. Lett.* **2012**, *108*, 074802. [CrossRef] [PubMed]
8. Asenjo-Garcia, A.; de Abajo, F.J.G. Dichroism in the interaction between vortex electron beams, plasmons, and molecules. *Phys. Rev. Lett.* **2014**, *113*, 066102. [CrossRef] [PubMed]
9. Harvey, T.; Pierce, J.; Chess, J.; McMorran, B. Demonstration of electron helical dichroism as a local probe of chirality. *arXiv* **2015**, arXiv:1507.01810. [CrossRef].
10. Serbo, V.; Ivanov, I.P.; Fritzsche, S.; Seipt, D.; Surzhykov, A. Scattering of twisted relativistic electrons by atoms. *Phys. Rev.* **2015**, *92*, 012705. [CrossRef]
11. Ivanov, I. Promises and challenges of high-energy vortex states collisions. *Prog. Part. Nucl. Phys.* **2022**, *127*, 103987. [CrossRef]
12. Campos, A.; Hatsagortsyan, K.; Keitel, C. Construction of dirac spinors for electron vortex beams in background electromagnetic fields. *Phys. Rev. Res.* **2021**, *3*, 013245. [CrossRef]
13. Moreau, J. Constantes d'un îlot tourbillonnaire en fluide parfait barotrope. *Comptes Rendus Hebd. Des Séances L'Académie Des Sci.* **1961**, *252*, 2810–2812. Available online: <https://zbmath.org/?q=an:0151.41703> (accessed on 1 March 2024).
14. Moffatt, H.K. The degree of knottedness of tangled vortex lines. *J. Fluid Mech.* **1969**, *35*, 117–129. [CrossRef]
15. Bini, D.; Mashhoon, B.; Obukhov, Y.N. Gravitomagnetic helicity. *Phys. Rev. D* **2022**, *105*, 064028. [CrossRef]
16. Lund, K.; Jardine, M.; Lehmann, L.T.; Mackay, D.H.; See, V.; Vidotto, A.A.; Donati, J.F.; Fares, R.; Folsom, C.P.; Jeffers, S.V.; et al. *Measuring Stellar Magnetic Helicity Density*. Oxford University Press: Oxford, UK, 2020. [CrossRef]
17. Moraitis, K.; Pariat, É.; Savcheva, A.; Valori, G. Computation of relative magnetic helicity in spherical coordinates. *Sol. Phys.* **2018**, *293*, 92. [CrossRef]
18. Alpeggiani, F.; Bliokh, K.Y.; Nori, F.; Kuipers, L. Electromagnetic helicity in complex media. *Phys. Rev. Lett.* **2018**, *120*, 243605. [CrossRef] [PubMed]
19. Büchner, J.; Pevtsov, A. Magnetic Helicity. *Adv. Space Res.* **2003**, *32*, 1817. Available online: <https://hdl.handle.net/11858/00-001M-0000-0014-EE71-0> (accessed on 1 March 2024).
20. Brown, M.; Canfield, R.; Field, G.; Kulsrud, R.; Pevtsov, A.; Rosner, R.; Seehafer, N. *Magnetic Helicity in Space and Laboratory Plasmas: Editorial Summary*; Geophysical Monograph-American Geophysical Union: Washington, WA, USA, 1999. [CrossRef]

21. Forbes, K.; Andrews, D. Optical orbital angular momentum: Twisted light and chirality. *Opt. Lett.* **2018**, *43*, 435–438. [[CrossRef](#)] [[PubMed](#)]
22. Koksai, K.; Babiker, M.; Lembessis, V.E.; Yuan, J. Chirality and helicity of linearly-polarised Laguerre–Gaussian beams of small beam waists. *Opt. Commun.* **2021**, *490*, 126907. [[CrossRef](#)]
23. Alsaawi, N.; Lembessis, V.E.; Lyras, A.; Babiker, M.; Yuan, J. Helicity of magnetic fields associated with non-relativistic electron vortex beam. *JPhysA* 2024, submitted. [[CrossRef](#)]
24. Bliokh, K.; Dennis, M.; Nori, F. Relativistic electron vortex beams: Angular momentum and spin–orbit interaction. *Phys. Rev. Lett.* **2011**, *107*, 174802. [[CrossRef](#)] [[PubMed](#)]
25. Barnett, S. Relativistic electron vortices. *Phys. Rev. Lett.* **2017**, *118*, 114802. [[CrossRef](#)] [[PubMed](#)]
26. Bialynicki-Birula, I.; Bialynicka-Birula, Z. Relativistic electron wave packets carrying angular momentum. *Phys. Rev. Lett.* **2017**, *118*, 114801. [[CrossRef](#)] [[PubMed](#)]
27. Lei, C.; Dong, G. Electromagnetic field of a relativistic electron vortex beam. *Chin. Phys. B* **2020**, *29*, 084102. [[CrossRef](#)]
28. Wan, W.; Chen, F.R.; Zhu, Y. Design of compact ultrafast microscopes for single-and multi-shot imaging with mev electrons. *Ultramicroscopy* **2018**, *194*, 143–153. [[CrossRef](#)] [[PubMed](#)]
29. Subramanian, K.; Brandenburg, A. Magnetic helicity density and its flux in weakly inhomogeneous turbulence. *Astrophys. J.* **2006**, *648*, 71. [[CrossRef](#)]
30. Berger, M.; Field, G. The topological properties of magnetic helicity. *J. Fluid Mech.* **1984**, *147*, 133–148. [[CrossRef](#)]
31. Potter, M.C. *Mathematical Methods in the Physical Sciences*; Prentice-Hall: Hoboken, NJ, USA, 1978. Available online: <https://books.google.com.sa/books?id=XIxQAAAAMAAJ> (accessed on 1 March 2024).
32. Genet, C. Chiral light–chiral matter interactions: An optical force perspective. *ACS Photonics* **2022**, *9*, 319–332. [[CrossRef](#)]
33. Koksai, K.; Babiker, M.; Lembessis, V.E.; Yuan, J. Hopf index and the helicity of elliptically polarized twisted light. *J. Opt. Soc. Am. B* **2022**, *39*, 459–466. [[CrossRef](#)]
34. Wan, K. *Quantum Mechanics: A Fundamental Approach*; Jenny Stanford Publishing: Dubai, United Arab Emirates, 2019. Available online: <https://www.routledge.com/Quantum-Mechanics-A-Fundamental-Approach/Wan/p/book/9789814774659> (accessed on 1 March 2024).

Disclaimer/Publisher’s Note: The statements, opinions and data contained in all publications are solely those of the individual author(s) and contributor(s) and not of MDPI and/or the editor(s). MDPI and/or the editor(s) disclaim responsibility for any injury to people or property resulting from any ideas, methods, instructions or products referred to in the content.